*Supplemental Information for*

# Unveiling the quasiparticle behaviour in the pressure-induced high-$T_c$ phase of an iron-chalcogenide superconductor

Z. Zajicek,[1,*] P. Reiss,[1,2,*] D. Graf,[3] J. C. A. Prentice,[4]

Y. Sadki,[1] A. A. Haghighirad,[1,5] and A. I. Coldea[1,†]

[1]*Clarendon Laboratory, Department of Physics,*

*University of Oxford, Parks Road, Oxford OX1 3PU, UK*

[2]*Max Planck Institute for Solid State Research, Heisenbergstr. 1, 70569 Stuttgart, Germany*

[3]*National High Magnetic Field Laboratory and Department of Physics,*

*Florida State University, Tallahassee, Florida 32306, USA*

[4]*Department of Materials, University of Oxford,*

*Parks Road, Oxford OX1 3PH, United Kingdom*

[5]*Institute for Quantum Materials and Technologies,*

*Karlsruhe Institute of Technology, 76021 Karlsruhe, Germany*

(Dated: 1 May 2024)

[*] These two authors contributed equally

[†] corresponding author:amalia.coldea@physics.ox.ac.uk

**Supplementary Table** I. **The parameters used in the Fermi surface simulation**. The parameters are extracted by comparing the experimental data to the expansion $k_F(\psi,\kappa) = k_{0,0} + k_{0,4}\cos 4\psi + k_{1,0}\cos\kappa$. The isotropic term is $k_{0,0}$, $k_{04}$ is a four-fold symmetric term that affects the in-plane anisotropy and $k_{1,0}$ describes the interplane distortion of the Fermi surface. In FeS, the electron pockets are larger but significantly warped with $k_{10} = -0.063$ for the outer electron pockets and $k_{10} = -0.02$ for the outer hole cylindrical pocket [1].

| | Electron | | | | | | Hole | | | |
|---|---|---|---|---|---|---|---|---|---|---|
| | Inner | | | Outer | | | Inner | | Outer | |
| $p$ (kbar) | $k_{00}$ | $k_{04}$ | $k_{10}$ | $k_{00}$ | $k_{04}$ | $k_{10}$ | $k_{00}$ | $k_{10}$ | $k_{00}$ | $k_{10}$ |
| 0 | 0.0575 | 0.005 | -0.0025 | 0.13 | -0.04 | -0.035 | 0.041 | -0.041 | 0.1365 | -0.0335 |
| 4.6 | 0.0625 | 0.005 | -0.004 | 0.14 | -0.04 | -0.035 | 0.043 | -0.043 | 0.148 | -0.0305 |
| 11 | 0.0675 | 0.005 | -0.007 | 0.1535 | -0.04 | -0.0355 | 0.0495 | -0.0495 | 0.1605 | -0.029 |
| 17 | 0.0725 | 0.005 | -0.011 | 0.163 | -0.04 | -0.037 | 0.0515 | -0.0515 | 0.171 | -0.02675 |
| 22 | 0.078 | 0.005 | -0.015 | 0.171475 | -0.04 | -0.0365 | 0.0566 | -0.0566 | 0.17975 | -0.025 |

**Supplementary Table** II. **The extracted Fermi surface parameters from quantum oscillations studies**. The effective masses are extracted using the Lifshitz-Kosevich formula [2], as shown in Fig. 9. The Fermi energy is estimated using $E_{\rm F} = \hbar k^2/(2m^*)$ and the Osanger relationship $F = \hbar(\pi k^2)/(2\pi {\rm e})$ for different applied pressures. Errors in frequency are estimated from the FFT peak widths. Errors in effective mass are standard deviations in the LK fits. Errors in Fermi energy are propagated from errors in frequencies and effective masses.

| $p$ | 0 kbar | | | 4.6 kbar | | | 11 kbar | | | 17 kbar | | | 22 kbar | | |
|---|---|---|---|---|---|---|---|---|---|---|---|---|---|---|---|
| Orbit | $F$ (T) | $m^*$ ($m_e$) | $E_{\rm F}$ (meV) | $F$ | $m^*$ | $E_{\rm F}$ | $F$ | $m^*$ | $E_{\rm F}$ | $F$ | $m^*$ | $E_{\rm F}$ | $F$ | $m^*$ | $E_{\rm F}$ |
| $\alpha_1$ | | | | 100(10) | | | 103(12) | | | 110(8) | | | 120 | | |
| $\alpha_2$ | 100(10) | | | 130(10) | | | 180(15) | | | 230(15) | | | 260 | | |
| $\chi$ | 237(6) | 2.3(2) | 11.7(10) | 276(5) | 2.1(2) | 15(2) | 347(10) | 2.0(2) | 20(2) | 408(4) | 2.0(2) | 24(2) | 453 | 1.9(2) | 28(2) |
| $\epsilon$ | | | | | | | 447(3) | 6.0(10) | 8.6(14) | 511(6) | 4.5(10) | 13(3) | 588 | 6.5(13) | 11(2) |
| $\beta$ | 359(4) | | | 483(6) | 3.7(2) | 15(1) | 610(8) | 4.05(20) | 18(1) | 732(10) | 4.2(2) | 20(1) | 835 | 4.5(3) | 22(2) |
| $2\chi$ | 470(15) | | | 572(6) | 3.8(3) | 18(1) | 719(10) | 3.6(4) | 23(2) | 828(12) | 3.4(2) | 28(2) | 930 | 3.4(5) | 32(5) |
| $\gamma$ | 873(24) | 5.8(15) | 18(5) | 1068 | | | 1158(18) | 4.1(5) | 33(4) | 1285(11) | | | 1376 | | |
| $\delta$ | 971(11) | 3.9(1) | 29(4) | 1091(7) | 3.8(3) | 33(3) | 1236(10) | 3.6(2) | 40(3) | 1343(5) | 3.5(2) | 44(3) | 1431 | 3.8(3) | 44(3) |

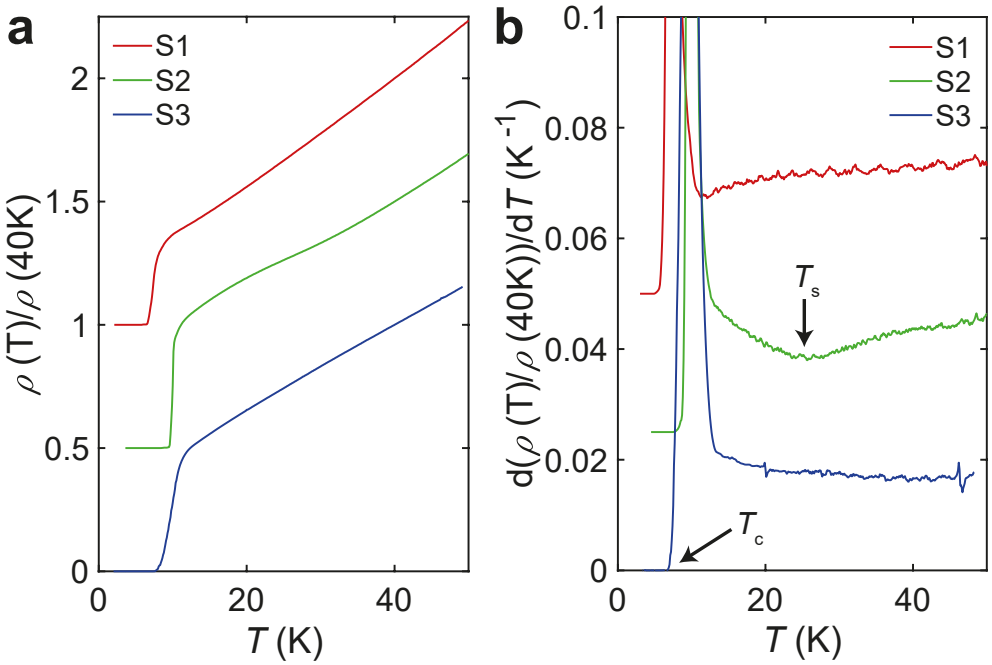


**Supplementary Figure** 1. **The low temperature resistivity for different crystals of $FeSe_{0.82}S_{0.18}$ from the same batch.** (a) The temperature dependence of the normalized resistivity at 40 K and (b) the corresponding first derivative of the resistivity for the different single crystals investigated for this study. The arrows indicate the position of the nematic transition $T_s$ for sample S2, and the superconducting transition $T_c$ for sample S3.

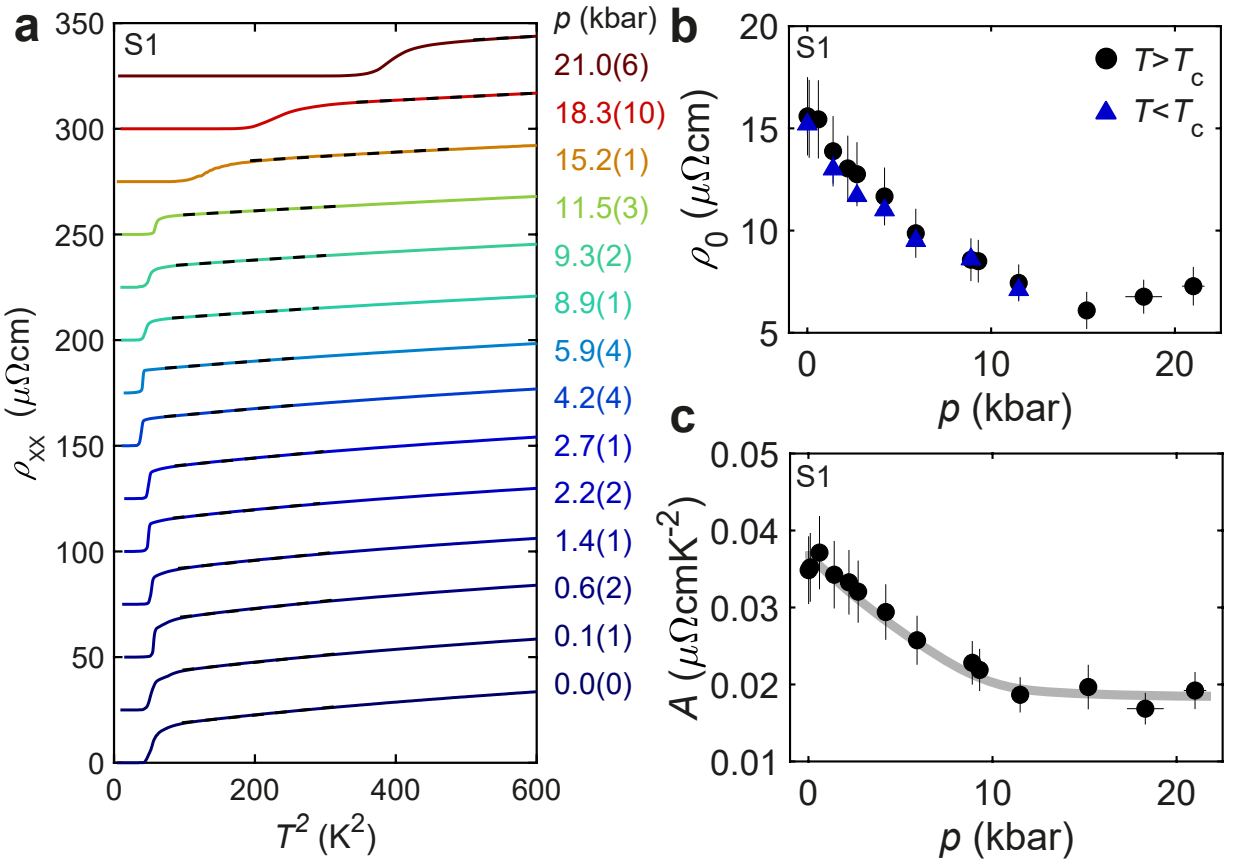


**Supplementary Figure** 2. **Low temperature Fermi liquid behaviour of $FeSe_{0.82}S_{0.18}$ for sample S1**. (a) The temperature dependence of resistivity at low temperature for sample S1. Curves are shifted vertically for clarity and the dashed lines are fits to a Fermi liquid behaviour, $\rho_0$+$AT^2$, over a limited temperature range ( $\Delta T \sim 8$ K) above the onset of superconducting transition ($T_{\rm on} + 2$ K). (b) Residual resistivity, $\rho_0$, extracted from the fits in (a) for $T > T_{\rm c}$. For $T < T_{\rm c}$, the low temperature resistivity is extrapolated from quadratic behaviour in magnetic field (see Fig. 12) before it is fitted to a Fermi liquid dependence. Error bars are standard deviations of linear fits to the resistivity. (c) The $A$ coefficient of the $T^2$ resistivity dependence as a function of pressure for sample S1. Error bars are standard deviations of the linear fits described in panel (a). Pressure error bars are from the width of the tin superconducting transition.

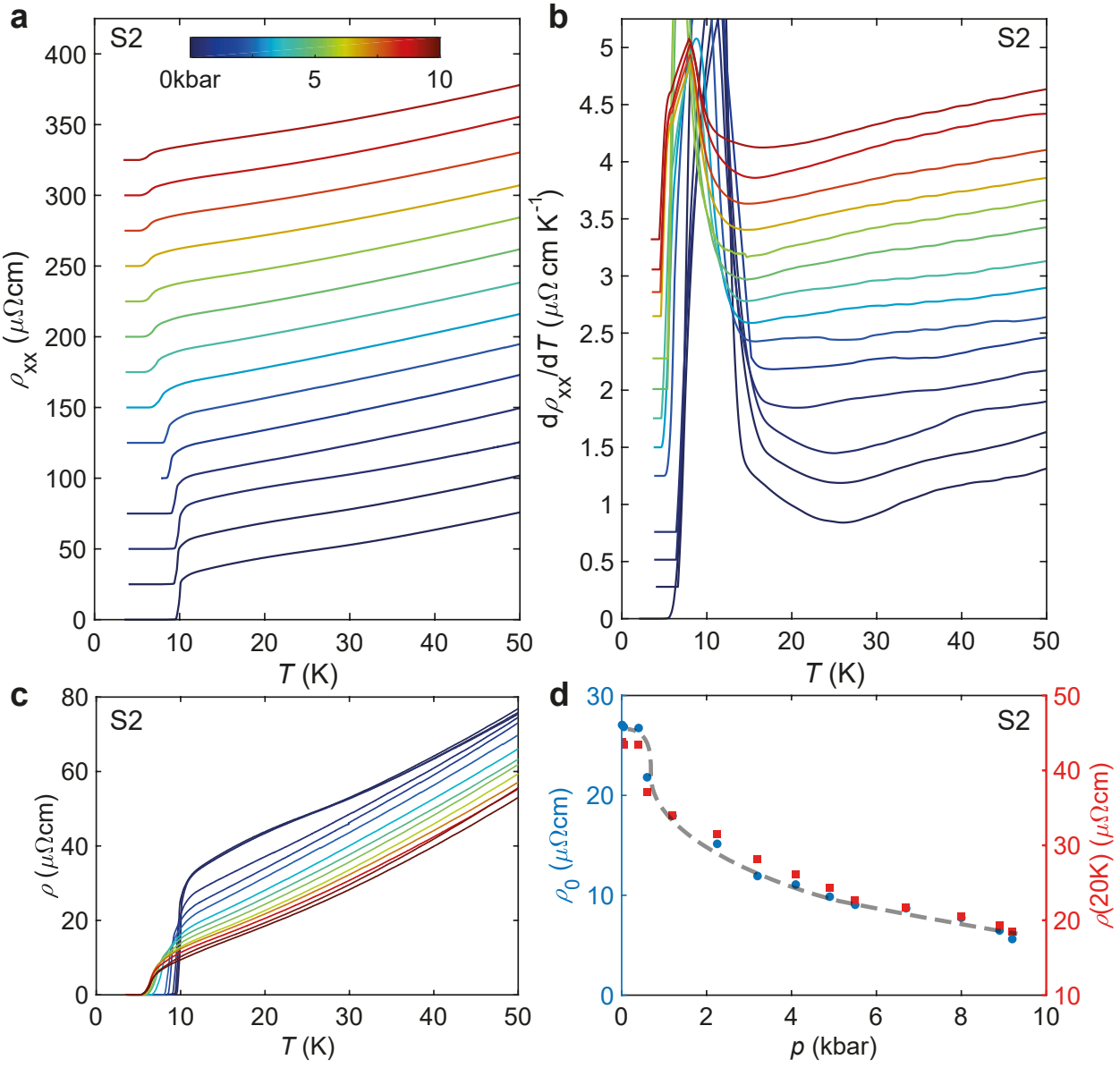


**Supplementary Figure** 3. **Transport properties under pressure of $FeSe_{0.82}S_{0.18}$ for sample S2.** (a) Temperature dependence of the resistivity up to 9 kbar and (b) the corresponding derivative used for determining the transition temperatures. Curves are shifted vertically for clarity. (c) The same as (a) without a vertical shift. (d) The resistivity extrapolated to zero temperature from a fit to the normal state resistivity above the onset of superconductivity, $\rho_0$ (blue circles, left vertical axis), and the value of resistivity at 20 K, (red squares, right vertical axis), as a function of applied pressure. The dashed line is a guide to the eye. The corresponding $A$ coefficient extracted from the $T^2$ dependence from panel (a) is plotted in Fig. 6.

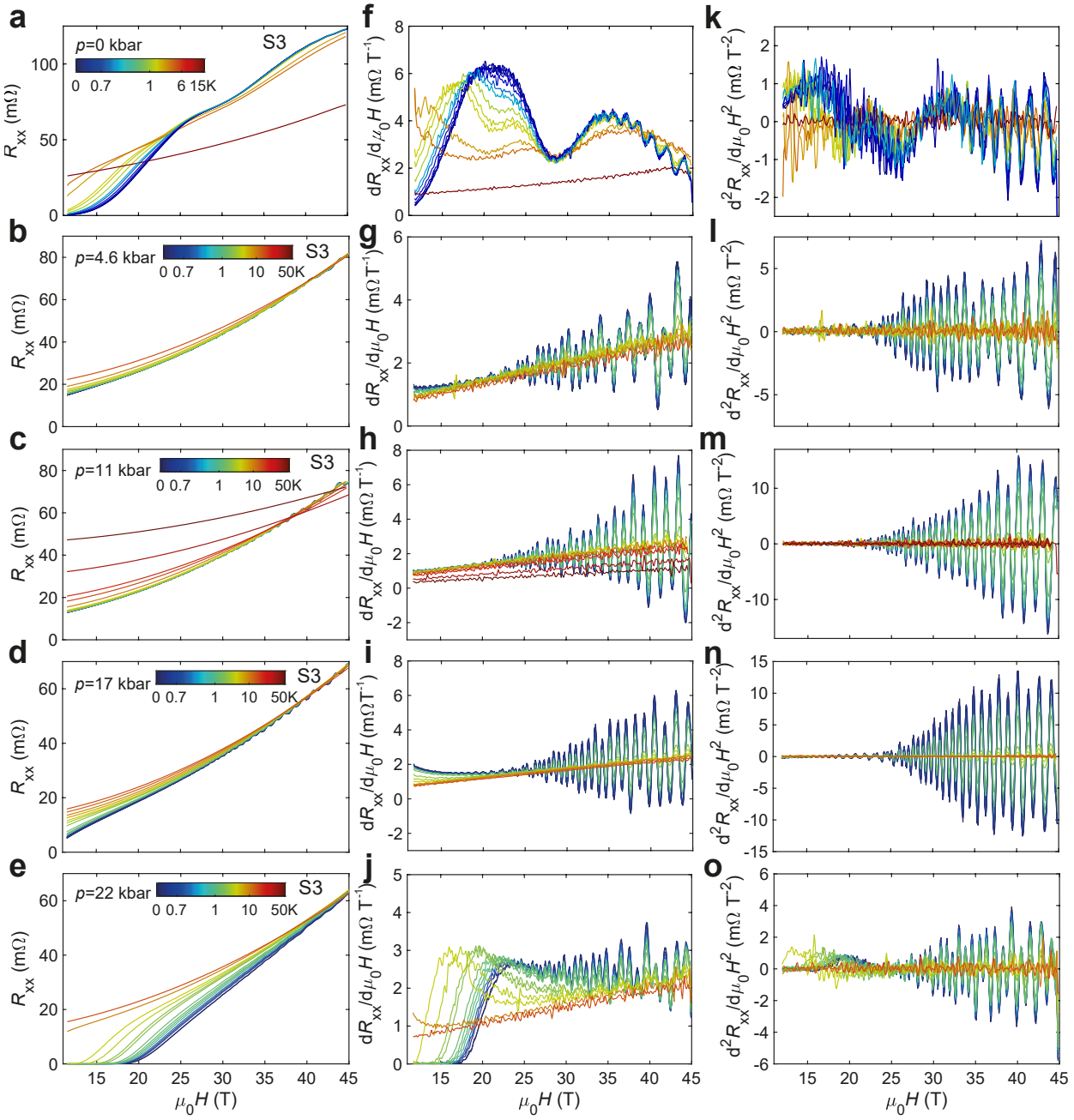


**Supplementary Figure** 4. **High-magnetic field longitudinal magnetoresistance of $FeSe_{0.82}S_{0.18}$ for sample S3.** The field dependence of the (a - e) magnetoresistance, (f - j) its first derivative in field, and (k - o) its second derivative in magnetic field. Each row corresponds to a different pressure, and the colour scale is used to define the temperature for each run applied across each row.

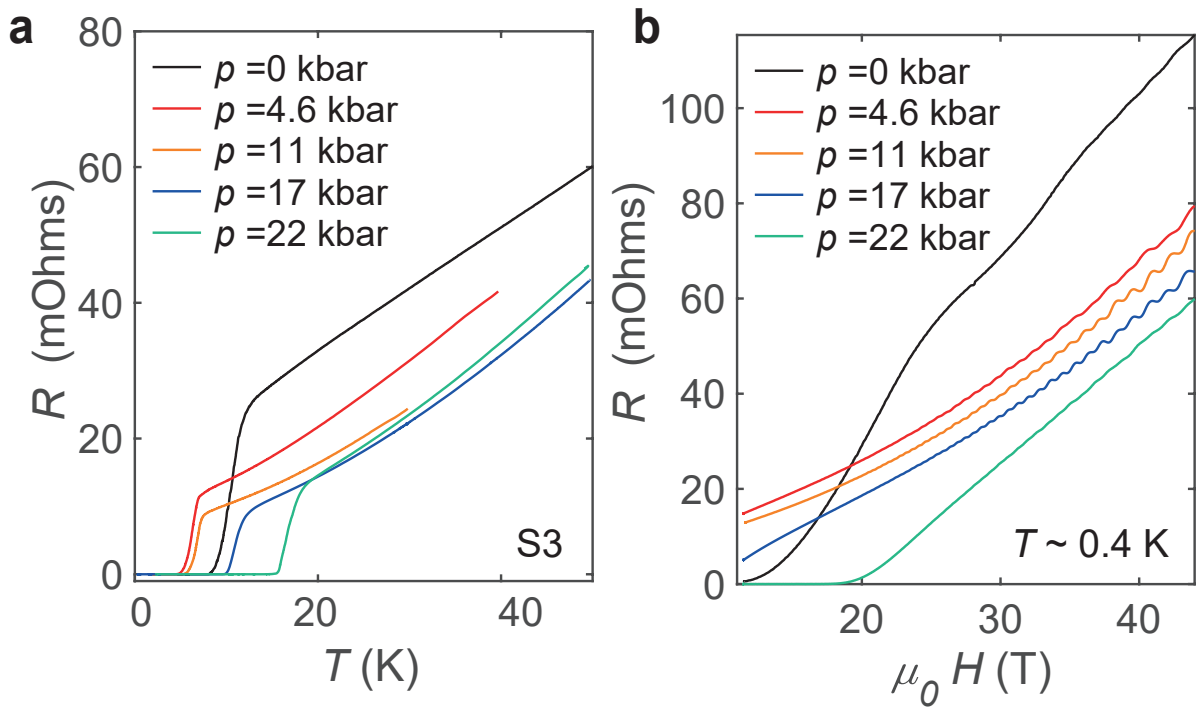


**Supplementary Figure** 5. **The transport properties of $FeSe_{0.82}S_{0.18}$ for sample S3.** (a) The low temperature resistance in zero-magnetic field and (b) the field-dependence magnetoresistance at 0.4 K for sample S3 measured at different applied pressures.

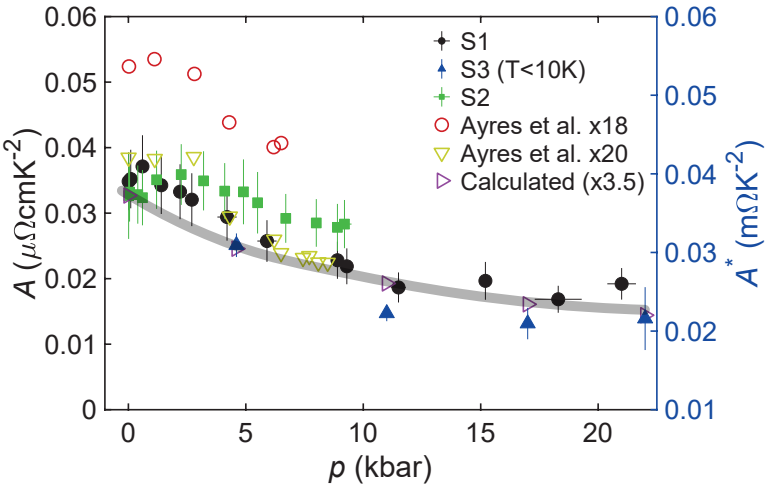


**Supplementary Figure 6. The pressure dependence of the $A$ coefficient.** The pressure dependence of the $A$ coefficient extracted from fitting to a low temperature Fermi liquid behaviour for different crystals and compared with $x$ = 0.18 and 0.20 from Ref. [3]. The $A$ values for samples S1 and S2 are estimated in zero field from a temperature range above the onset of superconductivity (Fig. 2 in the SM). The $A^*$ values for sample S3 values are extracted from resistance below 10 K and are plotted on the right axis (Fig. 7). Calculated $A$ values use $A \sim (\sum_i k_{\mathrm{F}_i}^3/m_i^{*2})^{-1}$ [4, 5] and the $k_{00}$ values from Table. I. The solid line is a guide to the eye for the calculated $A$ values. Error bars are standard deviations from the fits. Pressure error bars are from the width of the tin superconducting transition.

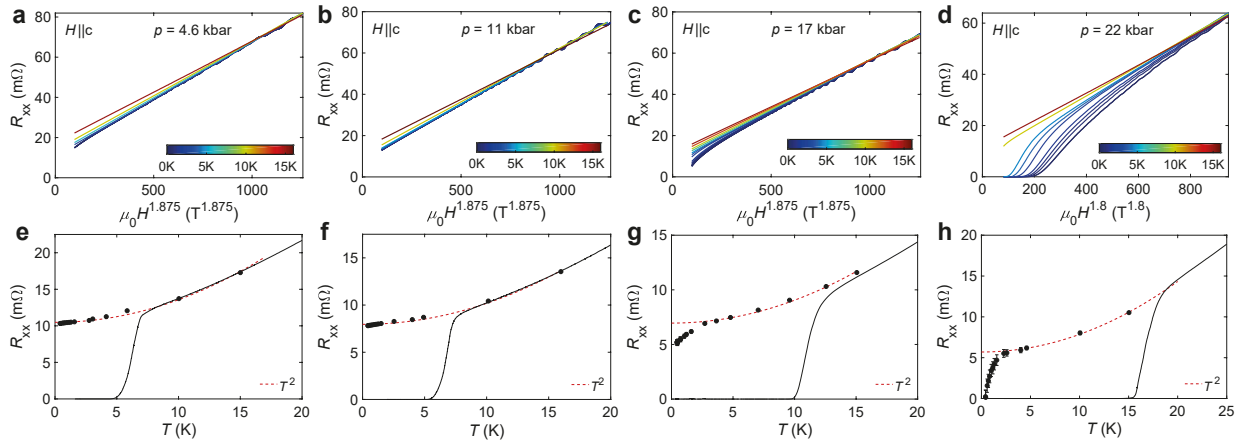


**Supplementary Figure 7. Magnetoresistance in magnetic field for $FeSe_{0.82}S_{0.18}$ for sample S3.** (a)-(d) The longitudinal resistivity, $\rho_{xx}$, as a function of $H^{1.875}$ field dependence for different applied pressures. (e)-(h) The zero field resistivity at low temperatures for each pressure (solid curve). Solid circles correspond to extrapolated zero field values at low temperatures from (a)-(d). Red dashed lines are fits at low temperature resistivity to a Fermi liquid $T^2$ dependence to extract the coefficient, $A^*$, shown in Fig. 6. Error bars in bottom panels are standard deviations from resistivity linear fitting in top panels.

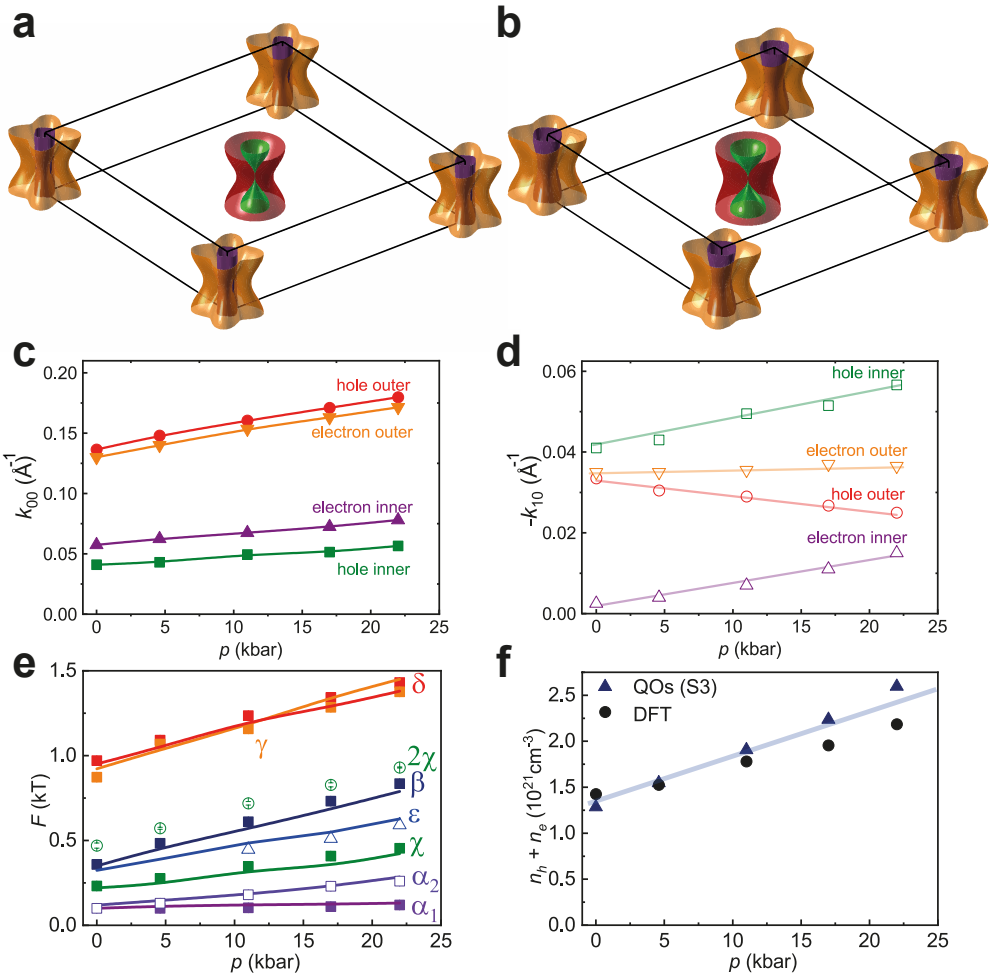


**Supplementary Figure** 8. **Modelling of the evolution of the Fermi surface of $FeSe_{0.82}S_{0.18}$ with pressure.** Fermi surface topography using the expansion $k_F(\psi, \kappa) = k_{0,0} + k_{0,4}\cos 4\psi + k_{1,0}\cos\kappa$ and matching the experimental parameters corresponding at (a) 0 kbar and (b) 22 kbar. The model expands the Fermi cylinders using symmetric parameters and match the observed frequencies and Fermi surface maps seen in ARPES [6], where the hole pocket suffers a Lifshitz transition [7]. The variation of the $k_{00}$ in (c) and $k_{10}$ parameters in (d) with applied pressure, as listed in Table I. Solid lines are guide to the eye. (e) The pressure dependence of the quantum oscillations frequencies from experiments (symbols) and the model (solid lines). Error bars are estimated from the width of the FFT peaks. (f) The estimation of the carrier density, $n$, using the Fermi surface model (solid triangles), and compared to the estimated values from shifted DFT calculations (solid circles).

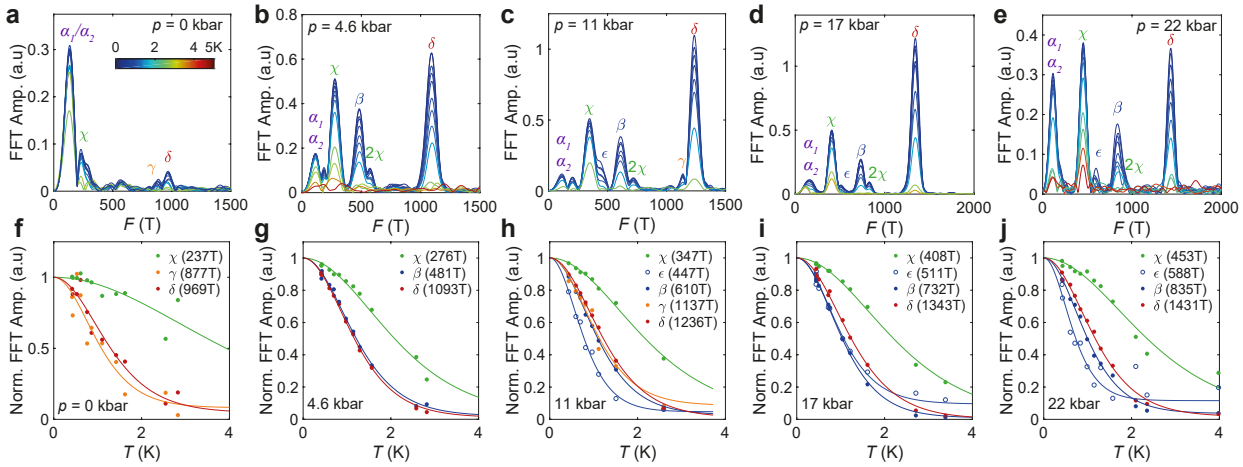


**Supplementary Figure** 9. **The determination of the quasiparticle effective masses.** (a-e) The temperature dependence of the Fast fourier frequency spectrum dependence for different pressures for sample S3 using a field window $\Delta B$=22 to 44.5 T and a Hanning window after a background of polynomial order 7 was removed. (f-j) The temperature dependence of the amplitude of the main peaks. The solid lines are fits to the Lifshitz-Kosevich formula which extracts the orbitally averaged effective mass of a particular orbit. and each plot is normalised to the base temperature for easier comparison. The main features correspond to hole pockets, $\chi, \beta$ and $\delta$ and the first harmonic of $\chi$ is clearly observed in most pressures, however, the $\epsilon$ and $\gamma$ pocket with heavier mass is much weaker.

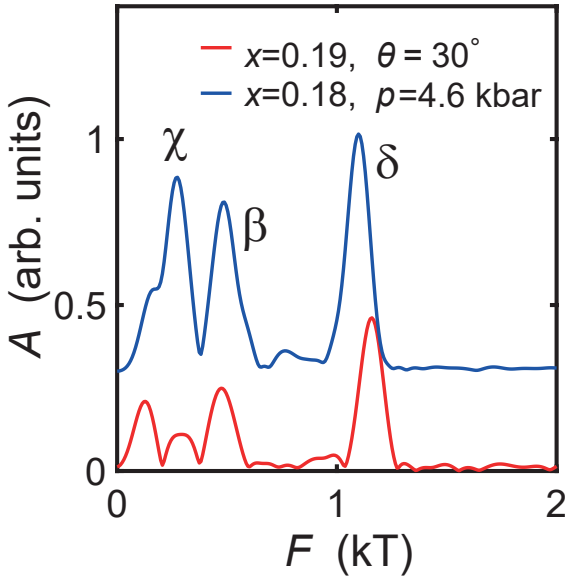


**Supplementary Figure** 10. **Comparison between the FFT spectra outside the nematic phase at** $T \sim 0.4$ **K.** The FFT spectra using the field window 25-45 T for $FeSe_{1-x}S_x$ for $x = 0.18$ at $p = 4.6$ kbar (top curve) and $x = 0.19$, $\theta = 30°$ (bottom curve) from Ref. [7].

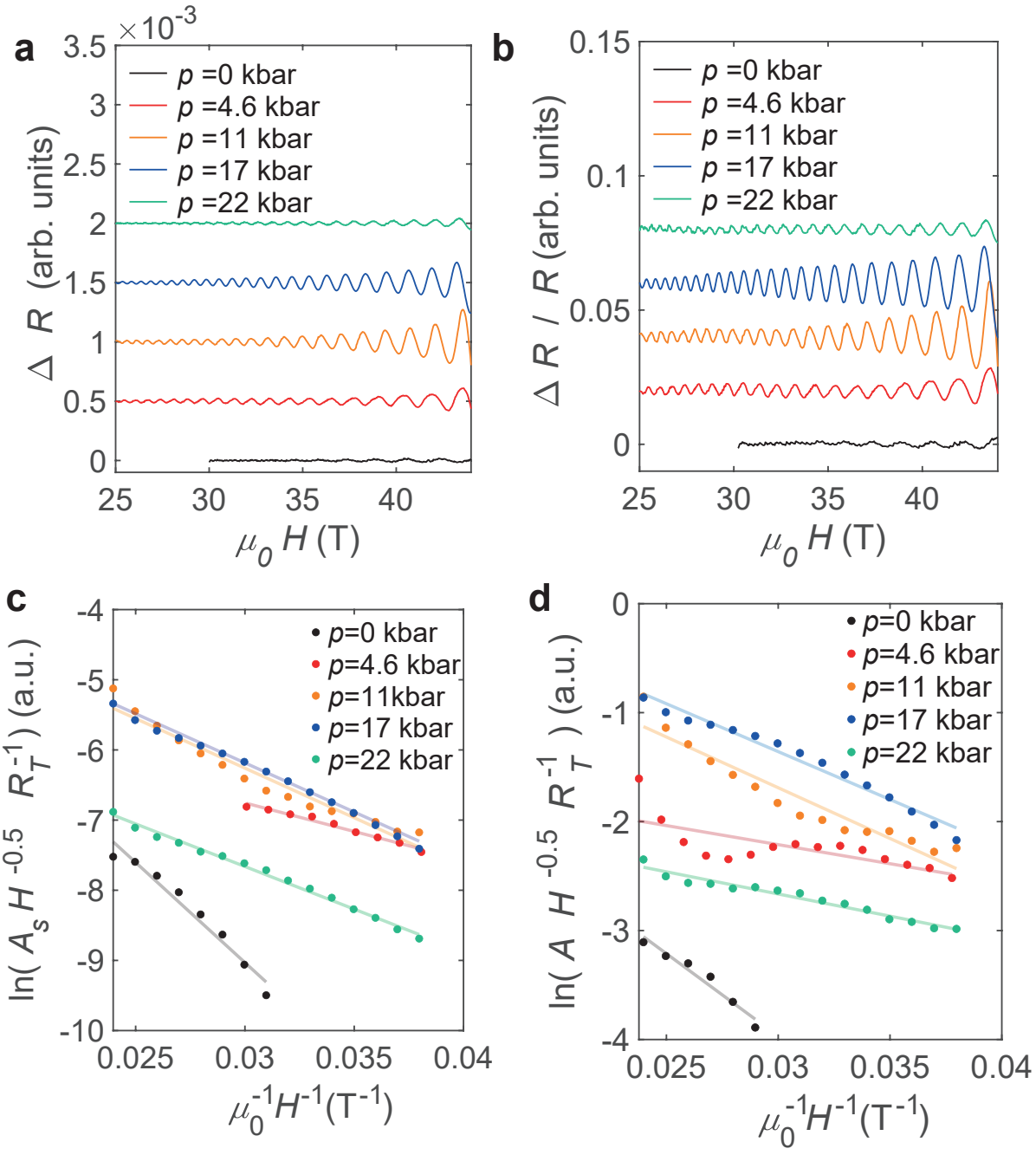


**Supplementary Figure** 11. **Dingle analysis of $\delta$ orbit.** Oscillatory part of the signal with a bandpass filter around the frequency of the largest orbit, $\delta$, as found from FFT spectra, obtained by subtracting a high order polynomial from the raw data, $\Delta R$ in (a) or additionally dividing the raw background $\Delta R/R$. The Dingle plots to extract the corresponding scattering times from (a) and (b) for the $\delta$ frequency at $\sim$ 0.4 K. Significant deviation from linear dependence is observed for 4.6 kbar, due to potential interference with $\gamma$ frequency.

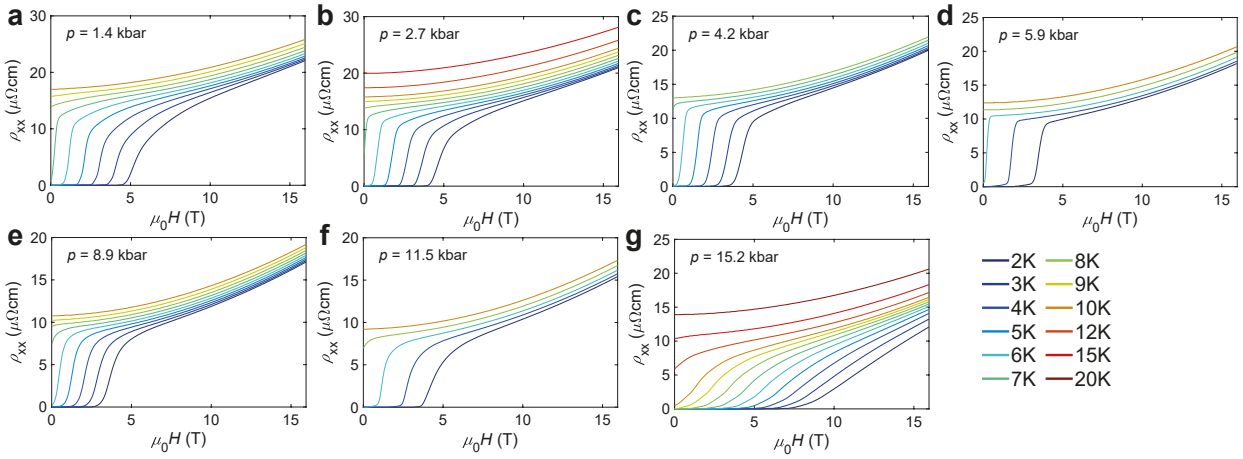


**Supplementary Figure** 12. **Low-magnetic field longitudinal resistivity for $FeSe_{0.82}S_{0.18}$ for sample S1.** (a)-(g) Longitudinal resistivity field dependence measured at fixed temperatures for different pressures. The transitions in magnetic field become broader at lowest temperature above 15 kbar in the region of the phase diagram where $T_c(p)$ increases fastest (1.2 K/kbar).

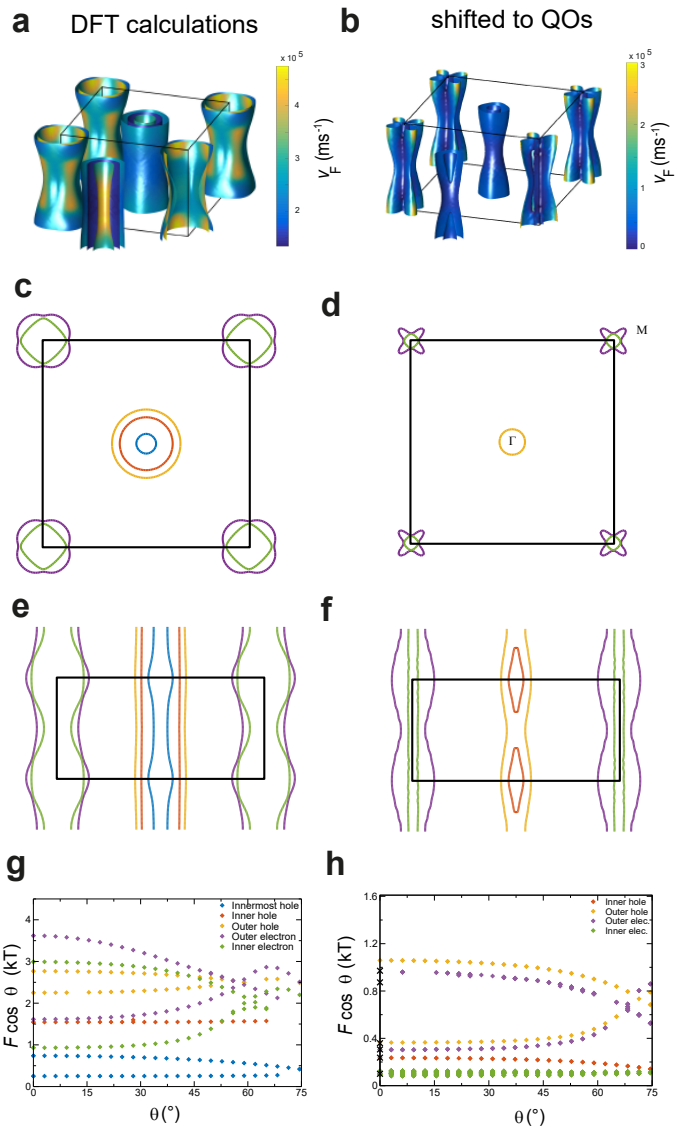


**Supplementary Figure** 13. **Fermi surface of $FeSe_{0.82}S_{0.18}$ from DFT calculations and the resulting one to match experimental data at ambient pressure.** Density functional theory (DFT) calculations were performed using Wien2k with the PBE functional (GGA approximation) for the non-magnetic case and including the spin-orbit coupling. We used the following lattice parameters $a = b = 3.754$ Å, $c = 5.442$ Åand $z$=0.266343, where $z$ is the position of the chalcogen atoms above Fe plane. (a) The three-dimensional representation of the Fermi surface from DFT calculations shows three cylindrical hole pockets in the centre of the Brillouin zone and two electron pockets at the corners. (b-c) The Fermi surface after applying shifts and renormalisation to match to the experimental data from quantum oscillations (QOs) in (b). (c-d) The Fermi surface cuts perpendicular to the c-axis at the centre of the Brillouin zone ($k_z = 0$) corresponding to the Fermi surfaces in (a-b). (e-f) The corresponding Fermi surface cuts along the $(110)$ plane and (g-h) the frequency rotation plots corresponding to the extremal areas on the Fermi surface from $B||c$ ($\theta = 0°$) towards $B||a$ ($\theta = 90°$). The shifted Fermi surface contains two electron and two hole pockets having mainly cylindrical shape except for the inner hole pocket which is a 3D pocket centred at $k_z = 0.5$. The electron pockets are cylindrical with different degree of in-plane and out-of-plane warping, with the outer electron pocket having a flower shape with four-fold symmetry and the inner electron pocket being a small and almost 2D cylinder.

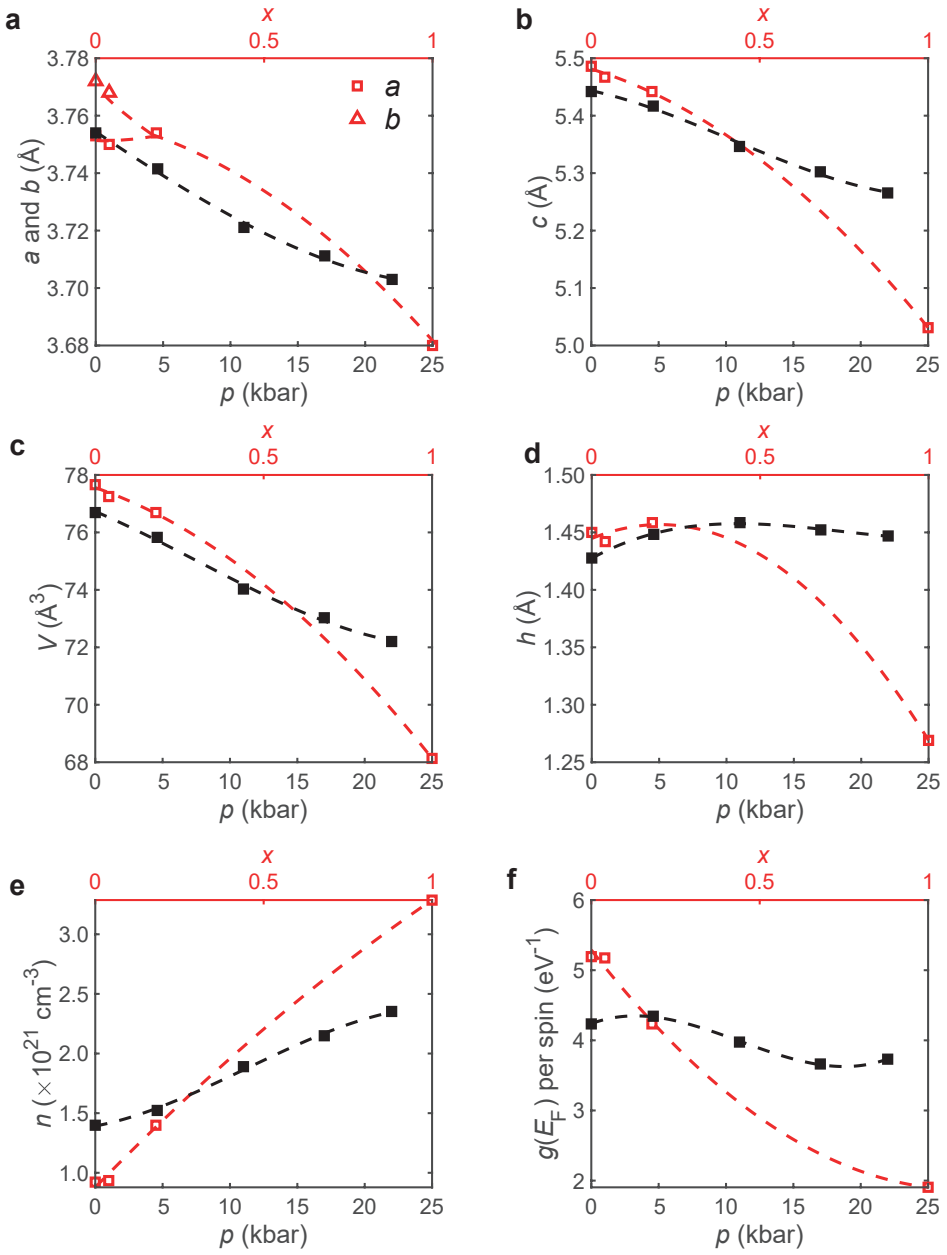


**Supplementary Figure** 14. **The evolution of the structural parameters as a function of hydrostatic pressure, $p$, and isovalent substitution, $x$ in FeSe$_{1-x}$S$_x$.** (a-d) Lattice constants $a$ (or $b$) (in panel a) and $c$ (panel b) as well as the volume of the unit cell $V$ (c) and the chalcogen height, $h = z \times c$ (d), as a function of S content, $x$ at ambient pressure (open red symbols, top axis), and as a function of applied pressure, $p$ for $x = 0.18$ (black squares, bottom axis) estimated using the same pressure trends as those for powder samples of $x = 0.2$ from Ref. [8]. (e-f) The trends of the estimated total carrier density (e) and the density of states at the Fermi level (f) as a function of $x$ and $p$ after shifting and renormalising the calculated electronic band structure to match experimental quantum oscillations data. DFT calculations assume that the chalcogen is populated by Se ions, and modify the lattice parameters and $z$ values, except for FeS, where S is the chalcogen.

[1] Bates, J. Fermi surface topology of iron-based superconductors. *MPhys project* (University of Oxford) (2022).

[2] Shoenberg, D. *Magnetic Oscillations in Metals* (Cambridge University Press, Cambridge, 1984).

[3] Ayres, J. *et al.* Transport evidence for decoupled nematic and magnetic criticality in iron chalcogenides. *Communications Physics* **5**, 100 (2022).

[4] Tsujii, M. *et al.* Charge Transport in $Ba_{1-x}Rb_xFe_2As_2$ Single Crystals. *Journal of the Physical Society of Japan* **91**, 104706 (2022).

[5] E. Hussey, N. Non-generality of the Kadowaki–Woods Ratio in Correlated Oxides. *Journal of the Physical Society of Japan* **74**, 1107–1110 (2005).

[6] Watson, M. D. *et al.* Suppression of orbital ordering by chemical pressure in $FeSe_{1-x}S_x$. *Phys. Rev. B* **92**, 121108 (2015).

[7] Coldea, A. I. *et al.* Evolution of the low-temperature Fermi surface of superconducting $FeSe_{1-x}S_x$ across a nematic phase transition. *npj Quantum Mater.* **4**, 2 (2019).

[8] Tomita, T. *et al.* Correlation between $T_c$ and Crystal Structure in S-Doped FeSe Superconductors under Pressure: Studied by X-ray Diffraction of $FeSe_{0.8}S_{0.2}$ at Low Temperatures. *Journal of the Physical Society of Japan* **84**, 024713 (2015).